

Bayesian inference of three-dimensional gas maps

I. Galactic CO

P. Mertsch¹ and A. Vittino¹

Institute for Theoretical Physics and Cosmology (TTK), RWTH Aachen University, Sommerfeldstr. 16, 52074 Aachen, Germany
e-mail: pmertsch@physik.rwth-aachen.de

January 1, 2021

ABSTRACT

Carbon monoxide (CO) is the best tracer of Galactic molecular hydrogen (H_2). Its lowest rotational emission lines are in the radio regime and thanks to Galactic rotation emission at different distances is Doppler shifted. For a given gas flow model the observed spectra can thus be deprojected along the line of sight to infer the gas distribution. We use the CO line survey of Dame et al. (2001) to reconstruct the three-dimensional density of H_2 . We consider the deprojection as a Bayesian variational inference problem. The posterior distribution of the gas densities allows us to estimate both the mean and uncertainty of the reconstructed density. Unlike most of the previous attempts, we take into account the correlations of gas on a variety of scales which allows curing some of the well-known pathologies, like fingers-of-god effects. Both gas flow models that we adopt incorporate a Galactic bar which induces radial motions in the inner few kiloparsecs and thus offers spectral resolution towards the Galactic centre. We compare our gas maps with those of earlier studies and characterise their statistical properties, e.g. the radial profile of the average surface mass density. We have made our three-dimensional gas maps and their uncertainties available to the community at this [https](https://www.rwth-aachen.de) URL.

Key words. Galaxy: structure – ISM: kinematics and dynamics – ISM: molecules – Methods: statistical

1. Introduction

Line surveys of molecular gas are a treasure trove for the study of the properties and dynamics of the interstellar medium (ISM Ferrière 2001). While the dominant fraction of molecular gas is molecular hydrogen (H_2), its line emission is inefficient in the cold and dense phase, due to the large spacing of its energy levels. The energy levels of carbon monoxide (CO), on the other hand, are much more closely spaced, rendering it radiatively more efficient in the same environments. To a first approximation, the density of H_2 and CO are linearly related, making CO the preferred proxy for H_2 . In particular the $J = 1 \rightarrow 0$ emission of ^{12}CO at 115 MHz has become the observable of choice in the study of the molecular ISM in the Galaxy. While ^{12}CO is almost always in the optically thick regime, the emission from its isotopologue ^{13}CO is in the optically thin regime, thus complementary (e.g. Szűcs et al. 2014), but still bright enough to allow mapping over large regions of the Galaxy (e.g. Schuller et al. 2021).

Ever since its observational discovery (Wilson et al. 1970), the coverage, sensitivity and angular resolution of CO surveys have continuously improved. Such surveys have enabled the study of the molecular ISM on scales as small as individual star-forming clumps of a few solar masses up to the total Galactic H_2 mass of the order of $10^9 M_\odot$. The applications of CO surveys are thus wide-ranging. Studies of galactic structure on the largest scales, in particular of features such as spiral arms or nuclear bars are interesting in their own right (Hou & Han 2014), but also offer invaluable clues for the theory of galaxy evolution (Kewley et al. 2019). The processes at play in the formation and dissolution of molecular clouds can be investigated through the study of individual clouds, but also the statistical analysis of cloud cata-

logues (e.g. Miville-Deschênes et al. 2017). As stellar nurseries, regions of dense molecular gas are central in the study of star formation (Kennicutt & Evans 2012). Due to its superior angular resolution compared to broad band emission in other wavelengths, the correlation between different emission processes relies on precise information on the molecular phases. One concrete example is diffuse emission produced by non-thermal cosmic rays (Ackermann et al. 2012). Here, the molecular gas (together with atomic gas) provides the target for high-energy cosmic rays, resulting in the production of non-thermal gamma-ray emission, either through bremsstrahlung or the production and subsequent decay of pions into high-energy gamma-rays and neutrinos. While the study of all such processes in the Galaxy is interesting in its own right it is also important to study and calibrate the correlations with other processes in order to use the observations of CO lines for extragalactic astrophysics (e.g. Sun et al. 2018).

Due to our vantage point in the Galaxy the galactic distribution of CO and H_2 is not readily available from the gas line surveys. However, due to Galactic rotation, different emission points along a line of sight in general possess different relative velocities with respect to the observer. Thus, the emission integrated along a line of sight consists of a spectrum that encodes the distribution of emission with distance. The data products of gas line surveys thus consist of spectra for individual lines of sight, oftentimes provided on a three-dimensional grid in longitude ℓ , latitude b and velocity with respect to the local standard of rest (LSR), v_{LSR} . For a given Galactic rotation curve or more generally given a gas flow model, such spectra can be deprojected *in principle* to find the three-dimensional distribution of CO and H_2 .

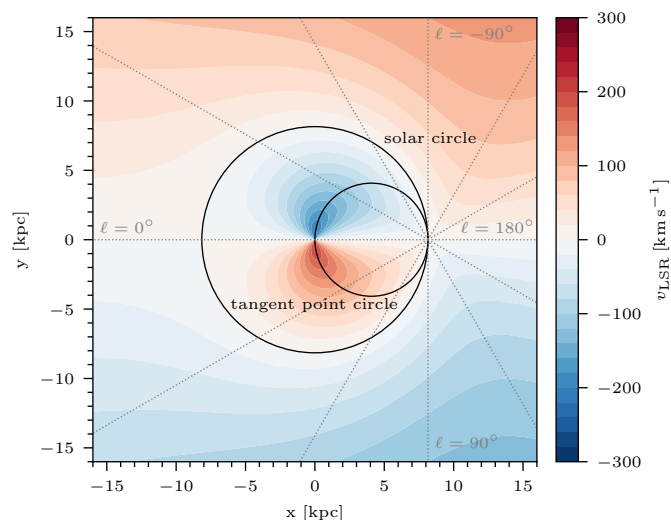


Fig. 1. Contour plot of the line of sight velocity v_{LSR} for positions (x, y) in the Galactic plane, assuming purely circular motions with speed $V(R) = 220 \text{ km s}^{-1}$. We also indicate lines of fixed longitude (dotted) and both, the solar circle and the tangent point circles.

Unfortunately, a couple of complications hamper the deprojection of the $l b v$ -cubes of gas line surveys into a three-dimensional xyz -cube of gas densities:

- Along a given line of sight and for a given velocity, most gas flow models exhibit two distance solutions inside the solar circle. For the velocity range affected by this effect, it is a priori unclear what fractions of the emission are residing at the near and far distances. This effect is commonly referred to as the near-far-ambiguity.
- For circular rotation, sight lines close to the Galactic centre (longitude $\ell \simeq 0^\circ$) and anti-centre (longitude $\ell \simeq \pm 180^\circ$) directions exhibit little to no radial velocity, thus lacking kinematical resolution: All emission piles up around $v_{\text{LSR}} = 0 \text{ km s}^{-1}$ and cannot be deprojected along the line of sight.
- Finally, peculiar velocities, that is random motions of gas on top of the large-scale gas flow, for instance due to stellar winds, supernova explosions or spiral structures, perturb the smooth mapping of distance to radial velocity. Such perturbations become visible as artefacts in the deprojected gas maps. Oftentimes, the distribution of gas gets smeared out along the line of sight, leading to the famous “finger-of-god” effect.

We illustrate the first two of these issues for the simple (and unrealistic) example of purely circular rotation. In this case, the radial velocity v_{LSR} along (ℓ, b) for emission from the galactocentric radius R is given by

$$v_{\text{LSR}}(R, \ell, b) = \cos b \sin \ell \left(\frac{R_\odot}{R} V(R) - V_\odot \right). \quad (1)$$

Further assuming a flat rotation curve, $V(R) = 220 \text{ km s}^{-1}$, we show v_{LSR} as a function of position in the Galactic plane ($b = 0^\circ$) in Fig. 1. We have assumed the observer to be located at Cartesian coordinates $(x, y) = (R_\odot, 0)$ with $R_\odot = 8.15 \text{ kpc}$ and the relation from longitude ℓ , latitude b and distance along the line of sight s to Cartesian coordinates x, y and z is

$$x = s \cos \ell \cos b - R_\odot, \quad (2)$$

$$y = s \sin \ell \cos b, \quad (3)$$

$$z = s \sin b. \quad (4)$$

The lack of kinematic resolution around the Galactic centre and anti-centre direction is readily visible: Each point along $\ell \simeq 0, \pm 180^\circ$ is observed without any Doppler shift, since there is no velocity component along the line of sight. It is also evident that the near-far-ambiguity only affects positions within the solar circle, the circle centred on the Galactic centre with radius R_\odot . Here, a given velocity $v_{\text{LSR}} < 0$ ($v_{\text{LSR}} > 0$) corresponds to two solutions for $-90^\circ < \ell < 0^\circ$ ($0^\circ < \ell < 90^\circ$). The two solutions are separated by the tangent point circle: a circle of radius $R_\odot/2$, centred at $(x, y) = (R_\odot/2, 0)$, the locus of points on the line of sight that are tangent to lines of constant v_{LSR} . Note that for a given line of sight the tangent point is an extremum of v_{LSR} .

There have been a number of previous attempts of deprojecting the results of gas line surveys into three-dimensional gas distributions and each study had to adopt a way for dealing with the issues discussed above. As for the lack of kinematic resolution towards the Galactic centre and anti-centre, Nakanishi & Sofue (2006) adopted a circular gas flow model, thus ruling out the possibility of directly reconstructing gas near $\ell = 0^\circ$ and $\ell = 180^\circ$. Instead, they resorted to interpolations between side-lines with small, but finite, radial velocities, at least for this side of the Galactic centre. The region beyond the Galactic centre with little to no kinematical resolution were excluded. Pohl et al. (2008) instead adopted the result of a numerical simulation (Bissantz et al. 2003) of the gas flow which includes non-circular motions. Towards the Galactic centre and anti-centre this provides several finite kinematic solutions, thus somehow aggravating the distance ambiguity, but also providing some kinematic resolution. Gas could thus be constructed also close to $\ell = 0^\circ$ and $\ell = \pm 180^\circ$ without interpolation.

As for the near-far-ambiguity, assuming an exponential or Gaussian distribution of gas in the direction perpendicular to the plane of the disk, the projection along the line of sight with a double-valued distance solution leads to a latitude profile that is composed of two Gaussians. Performing fits to the latitude distribution in individual velocity bins, thus allows to determine the relative distribution of gas between the two distance solutions. This method is known as the double Gaussian method and a number of studies have adopted this technique (e.g. Clemens et al. 1988). Both Nakanishi & Sofue (2006) and Pohl et al. (2008) have also used the double Gaussian method to break the near-far degeneracy in their deprojection. Specifically, Pohl et al. (2008) iteratively deprojected limited velocity ranges, assuming a certain thermal width, until the residual velocity spectra were in agreement with observational noise. Yet, some artefacts are clearly present in their gas maps. Nakanishi & Sofue (2006), on the other hand, managed to suppress some potential artefacts, but at the cost of adopting a rather coarse resolution, given the level of detail and small-scale structure available in the CfA CO survey compilation.

An alternative to the deprojection that manages to evade the above mentioned problems to a certain degree is forward modelling. For this, a parametric model for the gas distribution needs to be produced. Recently, Jóhannesson et al. (2018) provided such models for atomic and molecular hydrogen and determined the free parameters by fits to existing survey data. Note that here both the near-far-ambiguity and the lack of kinematic resolution are fixed by assuming a coherent distribution of gas across the offending regions. The authors managed to constrain a large number of parameters by their fit and the properties of the spiral arms bear some resemblance due to other, complementary data sets. However, as the authors admit themselves, not all the gas implied from the survey data can be successfully deprojected such

that the gas maps are to be considered as a lower limit of the real gas maps.

An important additional physical constraint that the gas densities have to fulfil but which is not leveraged by any of the previous studies is the existence of correlations. Such correlations must exist on a range of scales, and are due to a variety of processes. On the largest scales, these are due to the large-scale structure of the disk and the spiral arms, thus ultimately consequences of the formation history and density waves (Shu 2016). On smaller scales, the correlations are determined by the turbulent nature of the interstellar medium (Kolmogorov 1941), affecting both the fluctuation of gas density and velocity as well as magnetic fields. Modelling the three-dimensional gas density as a (Gaussian) random field, these correlation can be parametrised by the power spectrum of gas densities. In fact, there is some support for the hypothesis of a log-normal random field Nordlund & Padoan (1999); Ostriker et al. (2001), thus we will consider the log of gas densities to behave like a Gaussian random field. Such a reconstruction problem for the gas density under the priors of a given correlation structure is most conveniently formulated in a Bayesian framework. We note that with a general enough inference method, the parameters for the power spectrum do not need to be assumed, but can be determined by the inference method together with the gas density. In addition, the Bayesian inference method provides not only an estimate of the gas density, but also quantifies its uncertainty. To our knowledge, none of the previous studies provided such an uncertainty estimate.

One would hope that taking into account the existence of correlations, one would be able to predict gas densities for regions for which data is less constraining, e.g. along $\ell = 0^\circ$ and $\ell = \pm 180^\circ$. The quality of the deprojected data for these regions will of course be reflected in an increased uncertainty for these regions. Additionally, it can help break the near-far-ambiguity: Due to the coherence on large scales, the two solutions with gas at different distances will not exhibit the same likelihood and the inference algorithm will thus be able to distinguish between those solutions. Finally, taking the presence of observational noise into account in our inference method naturally allows denoising the observations.

The remainder of this paper is organised as follows: In Sec. 2, we briefly review the survey data used, introduce the two gas flow models we adopt and present the Bayesian method adopted for the deprojection as well as our data model. Our results are shown in Sec. 3 in a variety of representations. We compare both our gas maps and supplemental results with those of previous studies. We conclude in Sec. 4 and provide some thoughts on future directions. Details and supplemental information on one of the gas flow models are provided in appendix A.

2. Method

2.1. Survey data

We are using the ^{12}CO ($1 \rightarrow 0$) line spectra as compiled by Dame et al. (2001). This comprises 37 individual surveys that were performed with two 1.2 meter millimeter wave telescopes operated at Columbia University in New York City, NY, at the Centre for Astrophysics in Harvard, MA, and at Cerro Tololo in Chile. Together, these surveys cover the entire Galactic plane in longitude, extending to $\pm 30^\circ$ in latitude, thus covering virtually all areas for which significant emission has been reported. The velocity range is from -319.8 to 319.8 km/s in velocity. Between individual surveys, the angular resolution varies from $1/16$ to

$1/2$, as does the rms noise level which we conservatively fix to 0.3 K per channel. The survey data were downloaded from the SAO Radio Telescope Data Centre¹.

Note that before publication the raw survey data had been corrected for the motion of the Earth and the Sun with respect to the LSR. Since the time of the publication of Dame et al. (2001), better estimates of these relative velocities have become available, however. Therefore we have corrected the survey data by taking into account the updated parameter values as described in Sec. 4.1 of Wenger et al. (2018), adopting the parameter values of a recent, parallax-based determination of the distances to ~ 200 masers (Reid et al. 2019). Specifically, we have converted the standard cartesian velocity component $(U, V, W) = (10, 15, 7)$ km/s of the original surveys with the values $(U', V', W') = (10.6, 10.7, 7.6)$ km/s of model A5 of Reid et al. (2019). In Fig. 2, we show two projections of the corrected $\ell b v$ -cube, that is integrated over velocity, the so-called zero-moment map (top panel) and integrated over latitude, the $\ell - v$ diagram (bottom panel). In particular the $\ell - v$ diagram nicely illustrates the coherent structures that will help cure some of the deficiencies of the usual deprojection techniques.

After the deprojection, we will convert from the inferred CO emissivity to H_2 gas density, adopting a linear relation between them. This relation is commonly assumed to exist between the H_2 column density N_{H_2} and the velocity-integrated CO brightness temperature $W_{\text{CO}} \equiv \int dv T_b$, $N_{\text{H}_2} = X_{\text{CO}} W_{\text{CO}}$, thus establishing the conversion factor X_{CO} . While the relative abundances of H_2 and CO depend on a number of local factors (e.g. density, temperature, metallicity) it is customary to adopt an average value of the order of 10^{20} molecules cm^{-2} $(\text{K km s}^{-1})^{-1}$. The value $X_{\text{CO}} = 2 \times 10^{20}$ molecules cm^{-2} $(\text{K km s}^{-1})^{-1}$ with an uncertainty of $\pm 30\%$ has been recommended (Bolatto et al. 2013). For a recent review of molecular gas surveys, see Heyer & Dame (2015).

2.2. Gas flow models

The distribution of CO brightness temperature in ℓ , b and v depends, apart from the three-dimensional gas density field that we wish to reconstruct, on the three-dimensional velocity field which is also unknown. While it might seem that the assumption of purely circular rotation is the most model-independent assumption possible, it is problematic in two ways: practically, as it does not provide any kinematic resolution towards the Galactic centre and anti-centre directions and factually, as the gas flow is known *not* to be purely circular in the inner Galaxy due to the well-established presence of the Galactic bar (Blitz & Spergel 1991) that induces radial motions in the inner few kiloparsec. While the existence of non-circular motions is qualitatively not challenged, the details are everything but certain. In order to estimate the systematic uncertainty due to this, we have adopted two gas flow models.

The first is the result of a smoothed particle hydrodynamics simulation (Bissantz et al. 2003, hereafter BEG03). Apart from the gravitational potential of bulge and bar, some assumptions were made about the presence of spiral arms, in particular a four-armed spiral structure was assumed. The resulting $\ell - v$ -diagrams exhibit some resemblance with the CO data, but clearly miss some of the finer structure of the Dame et al. (2001) composite survey. We show their distribution of radial velocities in the top panel of Fig. 3. Here, we have extended the gas flow model with a flat rotation curve beyond 8 kpc, in a similar fashion as Pohl

¹ <https://www.cfa.harvard.edu/rtdc/>

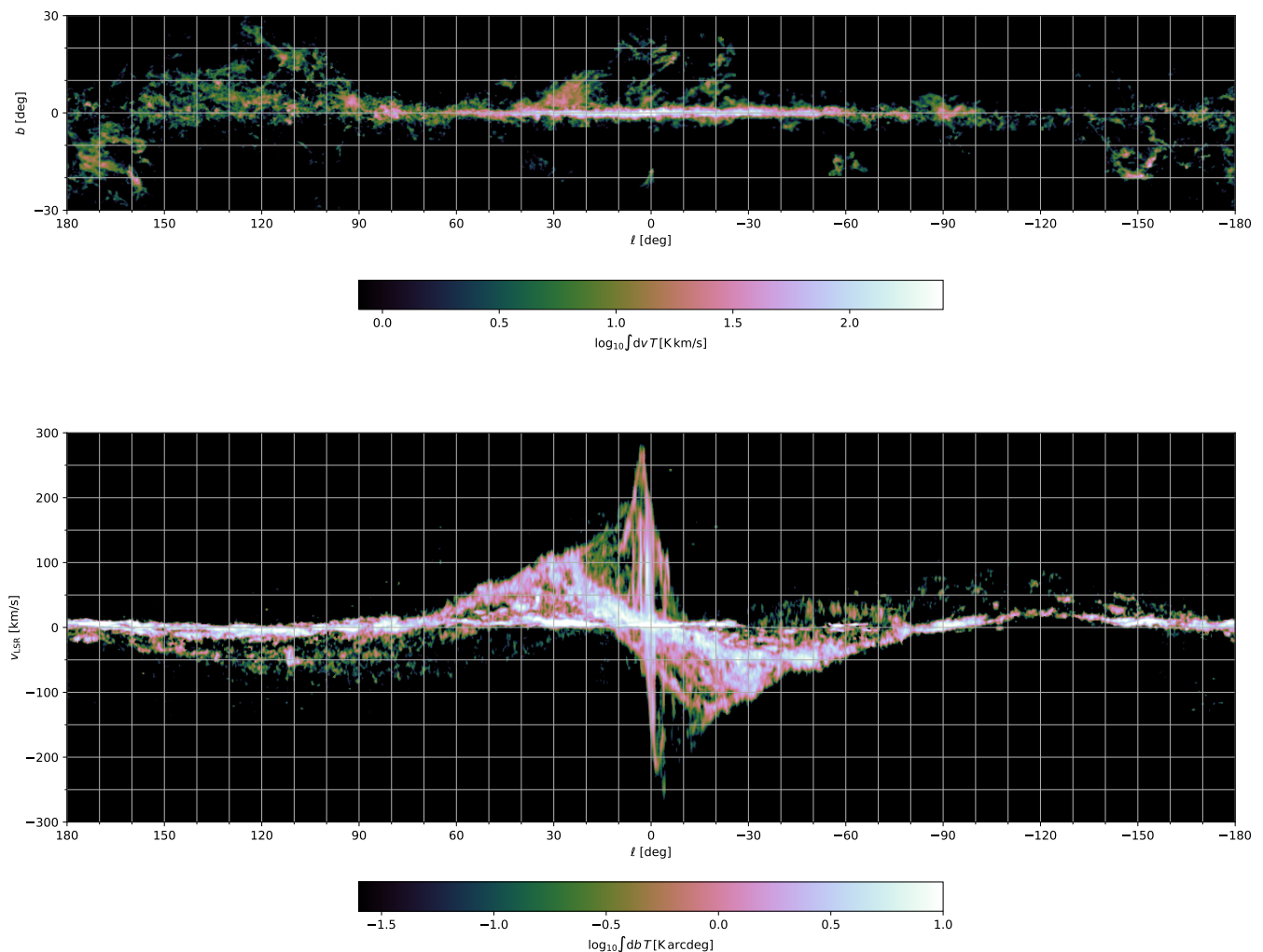


Fig. 2. **Top:** Velocity-integrated skymap of Galactic CO emission from the Dame et al. (2001) compilation of surveys, after correcting for the updated local parameters. **Bottom:** l - v -diagram of Galactic CO emission, integrated over latitudes from -30° to 30° , after correcting for the updated local parameters.

et al. (2008). The assumed presence of the spiral arms is clearly visible in gradients in the velocity field. While newer simulations are available (e.g. Baba et al. 2010; Pettitt et al. 2014) we have focussed here on BEG03 to allow for our results to be contrasted with the ones by Pohl et al. (2008) who used the same gas flow model.

In addition we have constructed a gas flow model based on a semi-analytical model for gas-carrying orbits in the potential dominated by the Galactic bar (Sormani et al. 2015). We provide details of our model in appendix A. In the middle panel of Fig. 3, we show the resulting radial velocity map as seen by an observer at a distance of 8.15 kpc from the Galactic centre (Reid et al. 2019) at an angle of 20° with respect to the major axis of the bar and moving with the velocity of the LSR. We also show the difference between the velocity fields of BEG03 and the SBM15 model in the bottom panel of Fig. 3. Three major differences are evident: First, while the overall agreement inside the solar circle is good, the agreement in the inner 2 kpc is less so. Second, the perturbations due to the spiral structure present in the model of BEG03 are clearly absent in our SBM15 model. The difference is mostly of the order of ± 10 km/s, but can be as large as ± 30 km/s in limited regions. Finally, outside the solar circle the

difference in the adopted rotation curves is marked and can lead to differences as large as ± 30 km/s. Note however that there is little molecular gas at the relevant distances.

2.3. Bayesian inference

In deprojecting gas line surveys, we follow two connected goals: First, we want to reconstruct the three-dimensional gas density under the constraint that the density possesses a certain spatial correlation structure. While we can be sure that such correlations exist, the details are not well-constrained and ideally we would hope for the data to constrain the correlation structure itself. Second, we would also like to obtain an estimate of the uncertainties. Both these goals are most directly achieved by adopting a Bayesian framework.

We consider the deprojection of the three-dimensional gas density from line survey data as a high-dimensional Bayesian inference problem, that is we are seeking the posterior distribution of the gas density for the given the survey data. According to Bayes' theorem (Bayes & Price 1763) the posterior is proportional to the likelihood, that is the probability for the observed brightness temperature given the gas density, times the

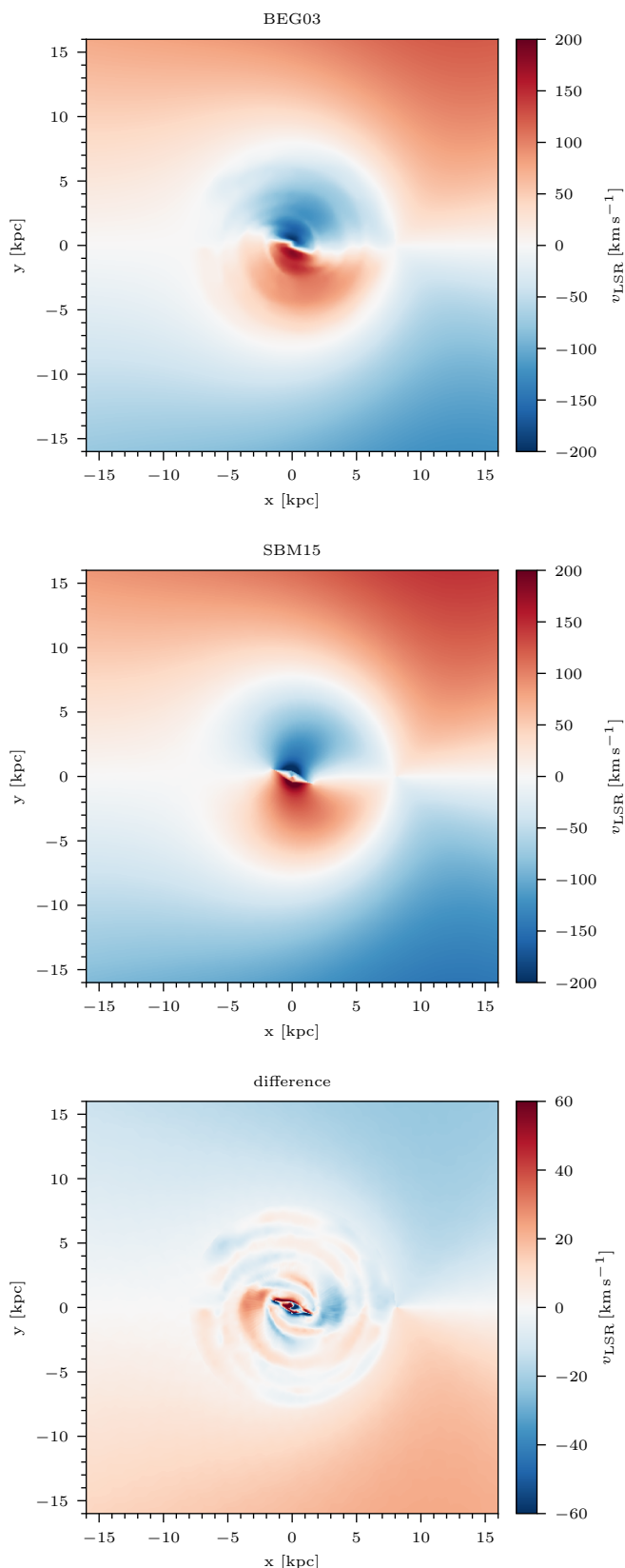


Fig. 3. Comparison of the two gas flow models that we adopted. **Top:** v_{LSR} for the BEG03 model. **Middle:** v_{LSR} for the SBM15 model. **Bottom:** Difference between v_{LSR} in the BEG03 and the SBM15 model. Note that the color scale is different in the bottom panel.

prior, that is the probability of the gas density. We could constrain ourselves to finding the maximum of the posterior, however, the maximum can be uninteresting if the posterior is multimodal or has degenerate directions. In addition, we would need to estimate the uncertainty separately, e.g. adopting the Laplace approximation (Laplace 1986) that equates the covariance at the maximum posterior position with the inverse Hessian. Instead, it is advantageous to keep track of the uncertainty while exploring the posterior.

Monte Carlo Markov Chain (MCMC) methods (Hastings 1970) do exactly that and they can approximate arbitrary posteriors given large enough sample sizes. However, with growing dimensionality, they become computationally expensive and for the large dimensionality of the current problem, prohibitively so. Variational inference (Blei et al. 2016) instead approximates the posterior with a parametric distribution, for instance a multivariate Gaussian. The parameters of the parametric distribution can be determined if the “distance” between the approximate distribution and the true posterior can be estimated, for instance through the Kullback-Leibler divergence (Kullback 1968). For a multi-variate Gaussian, this would in principle involve the inversion of the large covariance matrix which is again computationally prohibitive. Instead, it has been suggested (Knollmüller & Enßlin 2019) to approximate the covariance with the inverse Fisher information metric, a method known as Metric Gaussian Variational Inference. This method has recently been applied to problems ranging from reconstruction of the three-dimensional dust density in the Galaxy from reddening data (Leike & Enßlin 2019) to radio interferometry (Arras et al. 2019).

In practice, this is implemented as an iterative scheme, alternating between estimating the covariance at the current mean and updating the mean for the current estimate of the covariance. Specifically, adopting standardisation of the parameters, the computation of the (inverse) Fisher information metric requires the Jacobian of the standardisation map. This can be obtained either analytically or numerically by automatic differentiation. The mean is estimated by minimising the Kullback-Leibler divergence with respect to the mean. Note that this does not require explicitly computing the covariance matrix, which would entail the inversion of the Fisher information metric. Instead, the Kullback-Leibler divergence can be estimated stochastically, that is by drawing samples from a Gaussian with said covariance, which can be implemented with implicit operators. The application of the covariance in drawing the samples constitutes a linear system that can be solved by using a conjugate gradient algorithm.

2.3.1. Data model

The relation between the CO emissivity $\varepsilon(x, y, z)$ that we want to reconstruct and the brightness temperature $T(\ell, b, \nu)$ from the Dame et al. (2001) survey is given by a linear map R from signal space (x, y, z) to data space (ℓ, b, ν) ,

$$R[\varepsilon](\ell, b, \nu) = \int_0^\infty ds \varepsilon(\mathbf{r}) \delta(\nu - v_{\text{LSR}}(\mathbf{r})) \Big|_{\mathbf{r}=\mathbf{r}(\ell, b, s)}, \quad (5)$$

with $\mathbf{r}(\ell, b, s)$ specified in eqs. (2) to (4) above. Setting $T = R[\varepsilon]$ would result in a deterministic likelihood $p(T|\varepsilon)$,

$$p(T_{\ell b \nu} | \varepsilon_{xyz}) = \delta(T_{\ell b \nu} - R[\varepsilon_{xyz}]), \quad (6)$$

but we have to take into account the presence of additive noise n , thus altering our data model to

$$T_{\ell b \nu} = R[\varepsilon_{xyz}] + n_{\ell b \nu}. \quad (7)$$

We assume this noise to be Gaussian distributed, $n \sim p(n) = \mathcal{G}(n, N)$, with covariance N that is diagonal in harmonic space, $\tilde{N} = 2\pi\sigma_n^2\delta(\mathbf{k} - \mathbf{k}')$, that is white noise. Given the properties of the individual surveys combined in Dame et al. (2001) we fix $\sigma_n = 0.3$ K. We marginalise over the noise, thus obtaining a Gaussian likelihood,

$$\tilde{p}(T_{\ell bv}|\varepsilon_{xyz}) = \int dn p(T_{\ell bv}|\varepsilon_{xyz}, n_{\ell bv})p(n_{\ell bv}) \quad (8)$$

$$= \int dn \delta(T_{\ell bv} - R[\varepsilon_{xyz}] - n_{\ell bv})\mathcal{G}(n, N). \quad (9)$$

Finally, we have to take into account the fact that the measured v can differ from the actual radial velocity \hat{v} of the emitting gas, e.g. due to thermal line width or turbulence. We take the difference $(v - \hat{v})$ to be normal distributed with variance σ_v^2 and fix $\sigma = 5$ km s⁻¹. In principle, this requires another marginalisation, but we approximate this through a smearing of the linear map R instead,

$$p(T_{\ell bv}|\varepsilon_{xyz}) \quad (10)$$

$$\equiv \int d\hat{v} \int dn \delta(T_{\ell b\hat{v}} - R[\varepsilon_{xyz}] - n_{\ell b\hat{v}})\mathcal{G}(n, N)\mathcal{G}(v - \hat{v}, \sigma_v^2) \quad (11)$$

$$\simeq \int dn \delta(T_{\ell bv} - R'[\varepsilon_{xyz}] - n_{\ell bv})\mathcal{G}(n, N) \quad (12)$$

$$= \mathcal{G}(T_{\ell bv} - R'[\varepsilon_{xyz}], N), \quad (13)$$

where

$$R'[\varepsilon_{xyz}] \equiv \int d\hat{v} \mathcal{G}(v - \hat{v}, \sigma_v^2)R[\varepsilon_{xyz}] \quad (14)$$

$$= \int_0^\infty ds \varepsilon(\mathbf{r}) \mathcal{G}(v - v_{\text{LSR}}(\mathbf{r}), \sigma_v^2) \Big|_{\mathbf{r}=\mathbf{r}(\ell, b, s)}. \quad (15)$$

To be able to define the posterior distribution, we still need to specify the signal prior. We model the CO emissivity $\varepsilon(\mathbf{r})$ as a log-normal distributed random field, that is $s(\mathbf{r}) \equiv \ln(\varepsilon(\mathbf{r})/\varepsilon_0)$ is normal distributed. Under the assumption that s is statistically homogeneous, i.e. the two-point correlation in configuration space, $\langle s(\mathbf{r})s(\mathbf{r}') \rangle$, is a function of the distance $|\mathbf{r} - \mathbf{r}'|$ only, the two-point correlation in the harmonic domain becomes ‘‘diagonal’’, that is $\langle \tilde{s}(\mathbf{k})\tilde{s}(\mathbf{k}') \rangle = 2\pi P(k)\delta(\mathbf{k} - \mathbf{k}')$ where $P(\mathbf{k})$ is the power spectrum. We further assume that the power spectrum $P(\mathbf{k})$ is isotropic, $P(\mathbf{k}) = P(k)$.

Instead of assuming a form for the power spectrum $P(k)$, we would like to determine it during the reconstruction as well. Following Leike & Enßlin (2019), we therefore adopt a statistical model for the power spectrum, with a Gaussian distributed normalisation y , a Gaussian distributed power law index m and add a Gaussian random field in $\log(k)$,

$$\sqrt{P(k)} = \exp[(\mu_y + \sigma_y\phi_y) + (\mu_m + \sigma_m\phi_m)\log(k)] \quad (16)$$

$$+ \mathcal{F}^{-1}\left\{\frac{a}{1 + t^2/t_0^2}\tau(t)\right\}. \quad (17)$$

Here, ϕ_y and ϕ_m are random variables and $\tau(t)$ a random field (in $\log(k)$) that are encoding the power spectrum and are reconstructed at the same time as the signal itself. \mathcal{F}^{-1} represents the inverse Fourier transform from the variable t that is the conjugate of $\log(k)$. The parameters, μ_y , σ_y , μ_m , σ_m , a and t_0 are meta-parameters and we have fixed them to the following values: $\mu_y = -13$, $\sigma_y = 0.1$, $\mu_m = -4$, $\sigma_m = 0.1$, $a = 1$ and $t_0 = 0.1$. We stress that the above representation of $P(k)$ is flexible enough

to closely approximate the true underlying power spectrum for k where the data is constraining enough; where it is not, the shape is interpolated or extrapolated.

Finally, assuming s to be a homogeneous random field must fail when the deviations from this assumption for the real gas density become too strong. This is certainly the case when considering the confinement of molecular gas to the Galactic plane. In order to not be biased in the reconstruction, we have scaled the log-normal signal field ε_{xyz} with an exponential profile in z , $\exp[-|z|/z_h]$. We have adjusted z_h to values such that the signal field ε_{xyz} averaged over different portions of the Galactic disk does not show strong gradients in the z -direction and found $z_h = 40$ pc to give satisfactory results. We have also tested a Gaussian profile $\exp[-z^2/(2\sigma_z^2)]$, but found the results to be virtually unchanged.

2.3.2. Details on the implementation

As we are performing our computations on a computer, the signal field is not a continuous field of gas densities, but rather a discretised version thereof. We adopt a Cartesian grid with the x , y and z -coordinates indexed with α, β, γ , that is $\varepsilon_{\alpha\beta\gamma} = \varepsilon(x_\alpha, y_\beta, z_\gamma)$. Specifically, we have considered a $512 \times 512 \times 16$ Cartesian grid stretching from -16 kpc to 16 kpc in the x - and y -directions and from -0.5 kpc to 0.5 kpc in the z -direction, thus achieving a spatial resolution of $1/16$ kpc = 62.5 pc.

Given that the data are the spectra from a binned survey, they are already discretised, that is $T_{ijk} = T(\ell_i, b_j, v_k)$. We have degraded the data from their native resolution on a $2880 \times 481 \times 493$ grid to a $1440 \times 241 \times 247$ grid. The discrete version of the linear map of eq. (5) is

$$R_{ijk}^{\alpha\beta\gamma} = \int d\ell db dv ds \frac{\varepsilon_{\alpha\beta\gamma}}{\Delta\ell\Delta b\Delta v} \theta(\text{if } \mathbf{r} \text{ in } \alpha\beta\gamma) \delta(v - v_{\text{LSR}}(\mathbf{r})) \Big|_{\mathbf{r}=\mathbf{r}_{ijk}}. \quad (18)$$

Our data model, eq. (7), can thus be represented by a multiplication with the sparse matrix $R_{ijk}^{\alpha\beta\gamma}$.

For a specific implementation of the Gaussian variational inference, we have made use of the `nifty5` package².

3. Results and Discussion

The main result of our analysis are the 3D gas maps obtained from the two gas flow models and the corresponding uncertainties. Our gas maps provide the highest resolution three-dimensional deprojections of CO gas line surveys to date with a number of robust and well-localised emission regions and should prove useful in the study of Galactic structure and diffuse emission. We make our maps available to the community³.

In Fig. 4 we show the projection of the H₂ density onto the Galactic plane and its standard deviation, both for the BEG2003 gas flow model (top panels) and the SBM15 gas flow model (bottom panels). For either gas flow model, the survey data have been successfully deprojected into localised clusters of emission. The total gas mass reconstructed is $1.1 \times 10^9 M_\odot$ for the BEG03 model and $1.6 \times 10^9 M_\odot$ for the SBM15 model.

Some elongated structures, spurs or spiral arm segments are immediately visible. Some of the structures are more easily visible for the BEG03 model than for the SBM15 model. For instance, the two vertical spurs stretching from $(x, y) = (4, -1)$ kpc to $(x, y) = (4, 3)$ kpc and from $(x, y) = (6, -1)$ kpc

² <https://gitlab.mpcdf.mpg.de/ift/nifty>

³ <http://dx.doi.org/10.5281/zenodo.4405437>

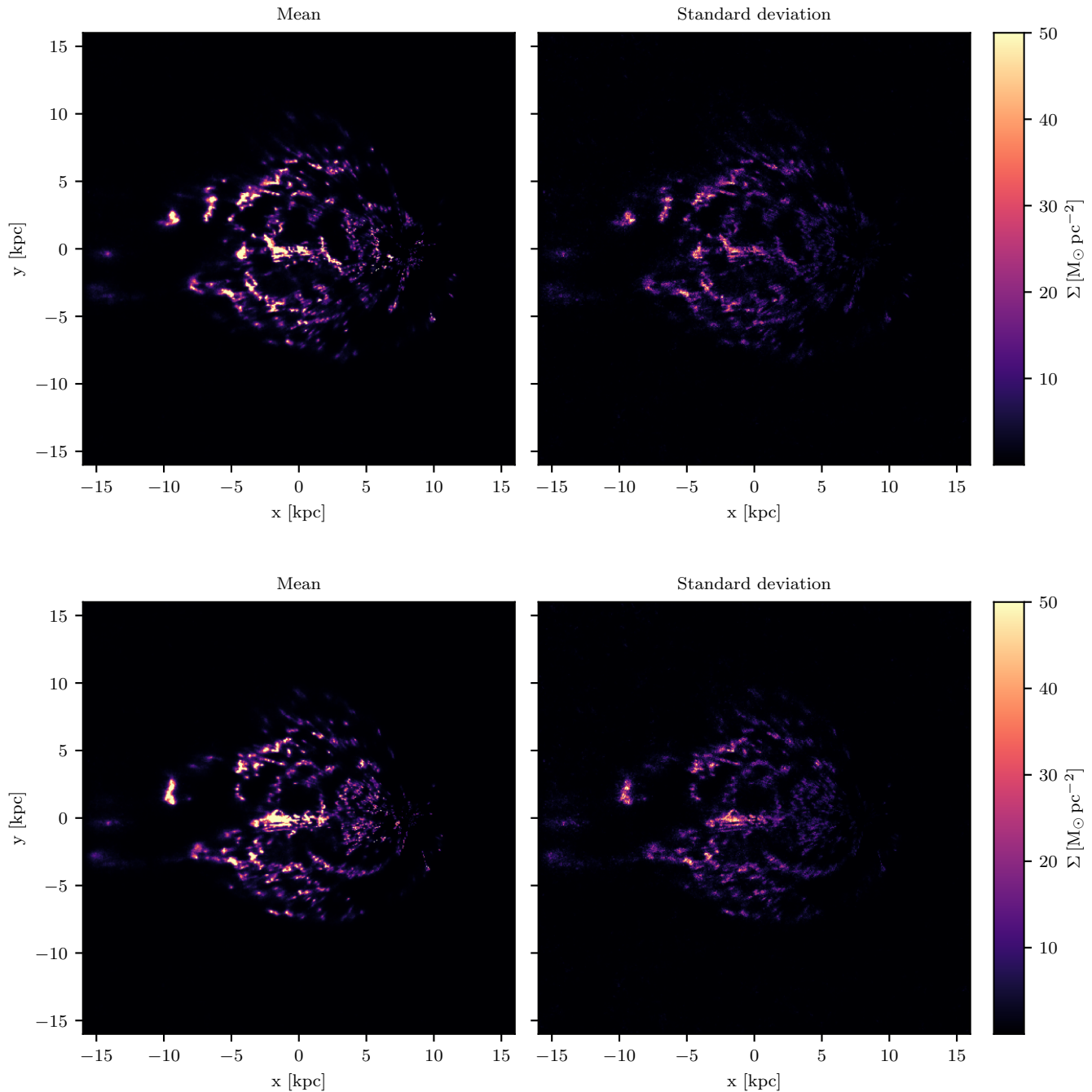


Fig. 4. Two-dimensional projection of reconstructed three-dimensional maps of molecular hydrogen. **Top left:** Mean gas surface density Σ for the BEG03 gas flow model. **Top right:** Standard deviation of the gas surface density Σ for the BEG03 gas flow model. **Bottom left:** Mean gas surface density Σ for the SBM15 model. **Bottom right:** Standard deviation of the gas surface density Σ for the SBM15 model.

to $(x, y) = (6, 3)$ kpc, respectively, are easily identified for the BEG03 model (top left panel of Fig. 4), but blend into a more extended emission for the SBM15 model. Revisiting Fig. 3 and in particular its bottom panel, it is clear that such structures are oftentimes linked to local extrema in the radial velocity field. For instance the two spurs discussed above coincide with maxima of the velocity field of the BEG03 model, but are absent in the SBM15 model. These are due to the spiral arms which have been put in by hand in the case of the BEG03 model, but not in the SBM15 model. We can also identify a spur that coincides with the tangent point circle, stretching from $(x, y) = (2, -3)$ kpc

to $(x, y) = (6, -4)$ kpc. This is likely an artefact pointing to too narrow a velocity range in the SBM15 model.

We note that the gas density comprises a rather large dynamical range as expected for a log-normal density. Some of the fainter features are therefore difficult to identify on a linear scale. In order to highlight them, we show the mean of the posterior, again projected onto the Galactic plane on a logarithmic colour scale in Fig. 5. We have also overlaid a longitude grid and the contours of the respective radial velocities. This should allow to more easily identify certain features with the corresponding features in the $\ell - v$ -diagram of Fig. 2.

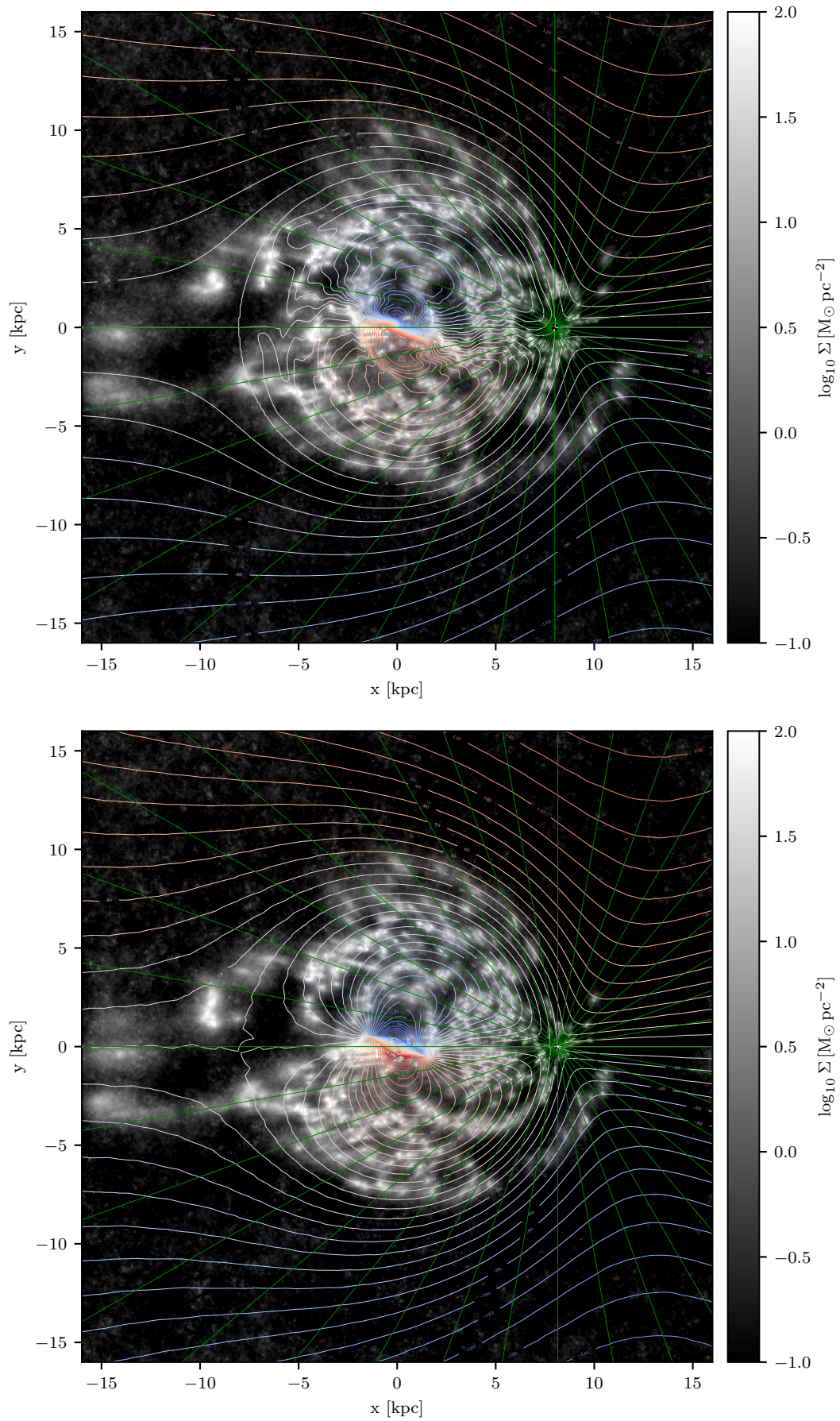


Fig. 5. Projected mean gas density Σ on a logarithmic colour scale, overlaying both contours in v_{LSR} and a grid in longitude. **Top:** For the BEG03 gas flow model. **Bottom:** For the SBM15 model.

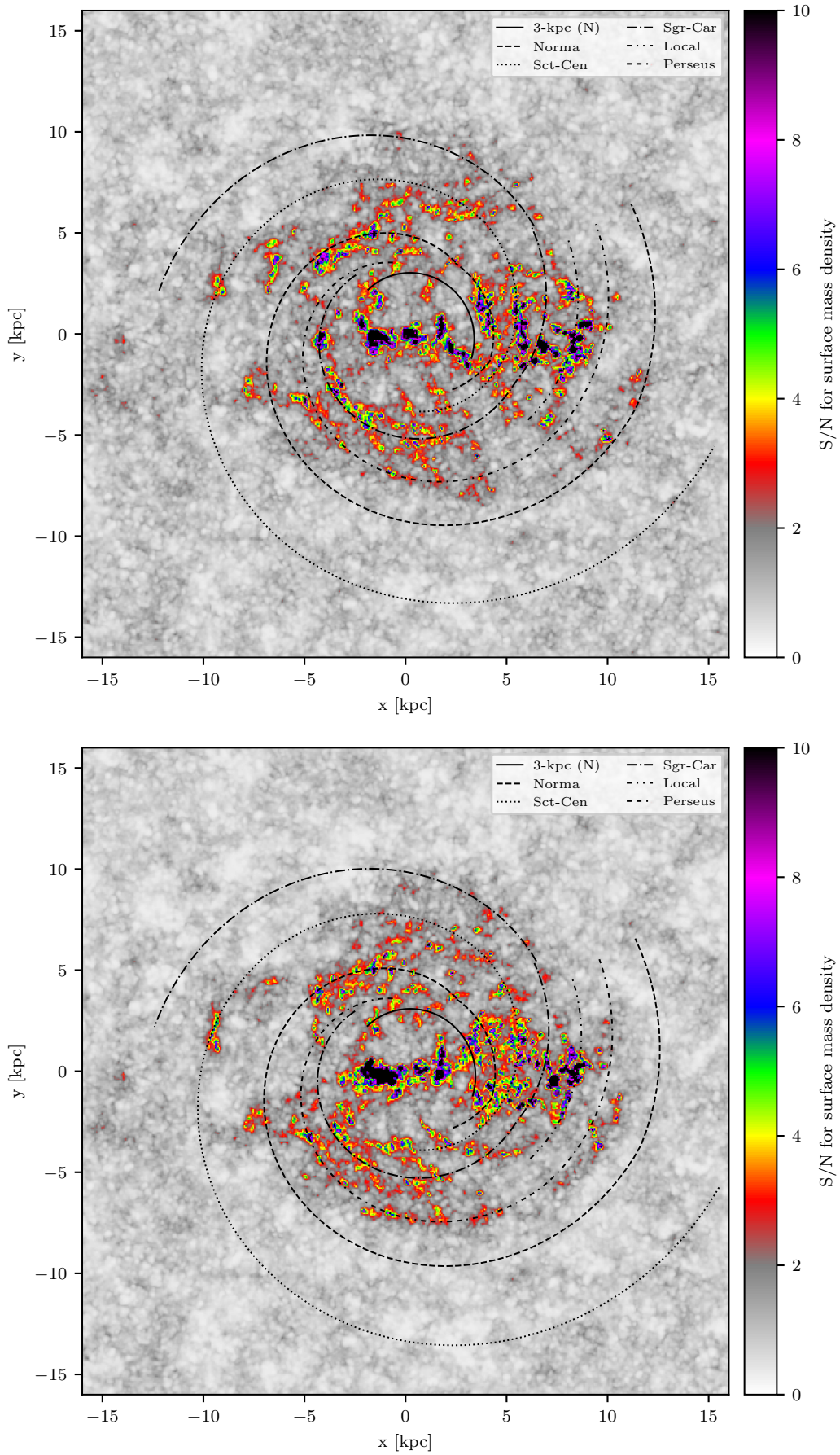


Fig. 6. Signal-to-noise ratio S/N of the mean gas density, with the spiral arms of Reid et al. (2019) overlaid. **Top:** For the BEG03 gas flow model. **Bottom:** For the SBM15 model.

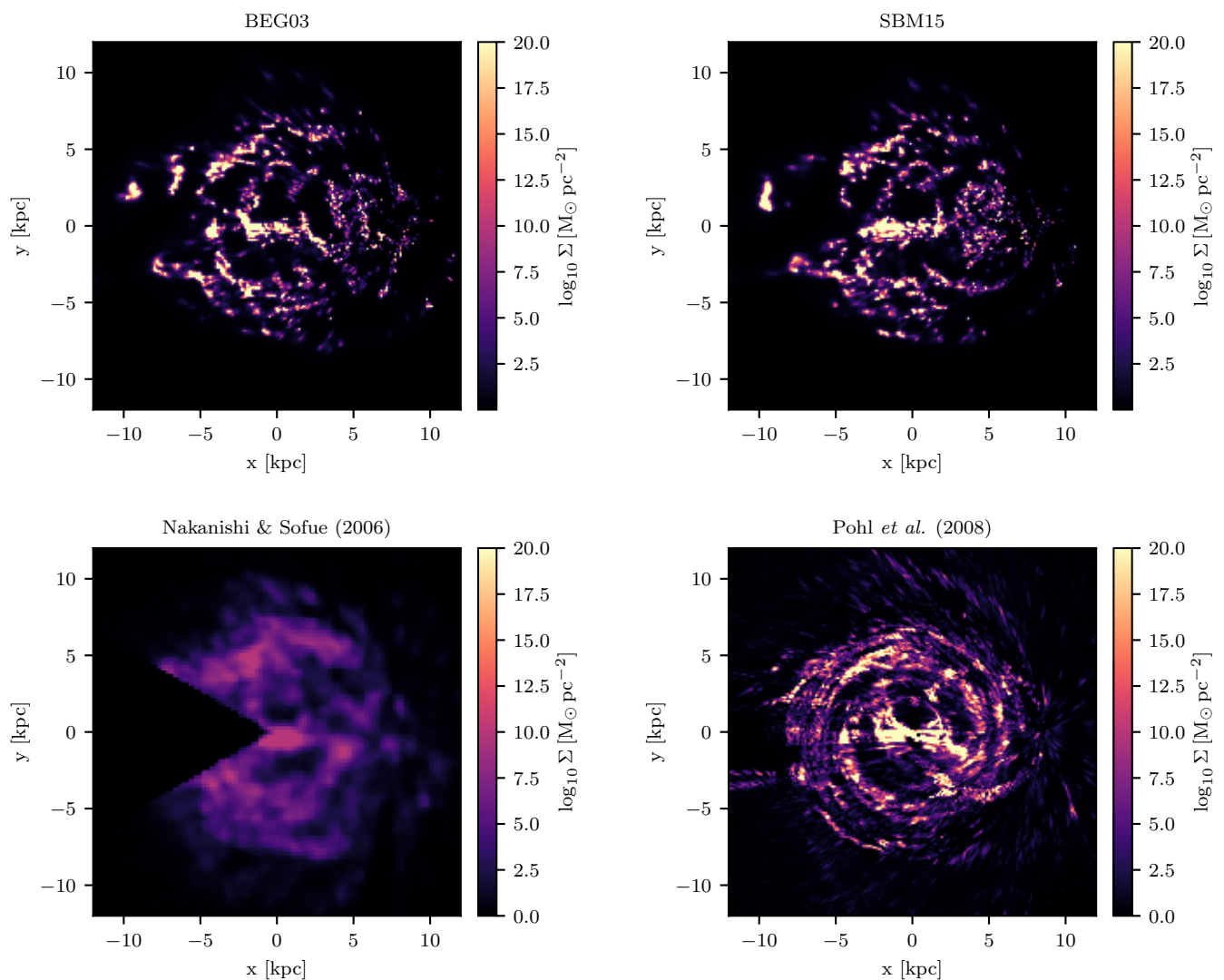


Fig. 7. Comparison of both our gas surface density constructions (top left and top right) with those of Nakanishi & Sofue (2006) (bottom left) and Pohl et al. (2008) (bottom right).

However, looking at the mean of the posterior alone can be misleading as some of the localised features also have a rather large uncertainty. Unlike the previous deprojections, however, we now have a means of judging the validity of certain features by comparing the mean μ of the posterior with its uncertainty σ . To this end, we define a signal-to-noise ratio (S/N) as μ/σ . We show S/N in Fig. 6, again for the BEG03 model in the top panel and in the bottom panel for the SBM15 model. One can clearly identify localised emission with a S/N ratio of 3 or higher. In Fig. 6, we have also overlaid the spiral arms, as determined from fits to a set of ~ 200 masers Reid et al. (2019). (See their Tbl. 2 for the fitted spiral parameters.) Many of the local emission features obtained for either gas flow model can be easily associated with a spiral arm: for the BEG03 model for all spiral arms, but most impressively for the Norma, Sagittarius-Carina, Local and Perseus arms. We comment on a couple of noteworthy differences and similarities between the significant features obtained for the BEG03 and the SBM15 models:

- The gas density in the SBM15 model is generally more scattered and does not cluster in regions as large as the emission

in the BEG03 model. This is again due to the presence of local extrema in the radial velocity field in the BEG03 model which boost the clustering. Such local extrema are all but absent in the SBM15 model and hence the gas density is less clustered.

- Yet, some of the spiral arms are obvious also for the SBM15 model, e.g. the segments along the Scutum-Centaurus and the Sagittarius-Carina arms for galacto-centric azimuths φ between $\sim 200^\circ$ and $\sim 280^\circ$. Other examples are the segments along the Norma ($90^\circ \lesssim \varphi \lesssim 150^\circ$), the local arm ($330^\circ \lesssim \varphi \lesssim 0^\circ$).
- Some emission, in particular beyond the solar circle, is placed at different distances in the BEG03 and SBM15 models due to the different rotation curves adopted here. Given the rather small velocity gradient, this easily translates into differences of the order of a kiloparsec and thus affects the association with spiral arms. One example is emission around $\ell \sim 110^\circ$ and with v_{LSR} between -60 and -50 km/s, see Fig. 2, bottom panel. With the BEG03 model, this emission is located around $(x, y) = (10, -6)$ kpc. With the SBM15 gas flow, this instead ends up at $(x, y) = (9.5, -5)$ kpc. In the

former case, an association with the Norma arm suggests itself, in the latter case, the association with the Perseus arm is more likely.

In Fig. 7, we revisit the mass surface densities obtained with either gas flow model (top panels) and compare them with the deprojections of Nakanishi & Sofue (2006) (bottom left) and Pohl et al. (2008) (bottom right). Note that all gas densities are shown with the same dynamical range, however, the mass surface density of Nakanishi & Sofue (2006) is significantly smoother. Some similarities are apparent between the map of Pohl et al. (2008) and our maps. This is even more so the case for our map that is based on the BEG03 model, the same gas flow model adopted by Pohl et al. (2008). However, there are also some differences:

- Spiral arms are more homogeneous in Pohl et al. (2008). While in our reconstruction, the width is oftentimes varying along the segments, in the gas density of Pohl et al. (2008), some ring segments appear to have constant width. This might be an artefact of the particular algorithmic reconstruction chosen there.
- An artefact, that is affecting both the Pohl et al. (2008) map and our SBM15 map is the emission concentrated along an arc of the tangent point circle (see discussion above).
- The peak in the gas density reconstructed for both our gas flow models near $(x, y) = (-9, 2)$ kpc is absent in the Pohl et al. (2008) map, possibly due to the chosen suppression at large galacto-centric radii.
- Another class of artefact, that is apparent in the Pohl et al. (2008) maps are the features elongated along the lines of sight, the so called “fingers of god”, especially in regions of low gas densities. These are almost completely absent in our reconstructions.
- Finally, Pohl et al. (2008) show some gas density in regions where we have found (almost) none, in particular beyond the solar circle. Unlike the structures solidly identified with spiral arms of the BEG03 model, some of these might actually be statistically not significant. This is to be compared with emission seen for our reconstruction in Fig. 5 near $(x, y) = (-14, -1)$ kpc and $(x, y) = (-14, -4)$ kpc which is not statistically significant, see Fig. 6.

We conclude our discussion by looking at some properties of the derived distributions in galacto-centric radius. In Fig. 8, we have plotted the surface mass density averaged in galacto-centric rings $R_i \leq R < R_{i+1}$ where $R_i = i\Delta R$ with $\Delta R = 0.5$ kpc. Close to the Galactic centre, the average gas density is a few tens of $M_\odot \text{pc}^{-2}$ and subsequently decreases towards $r \approx 3$ kpc. Beyond, there is a local maximum at $r \approx 5$ kpc, the well-established molecular ring (or possibly a convergence of spiral arms Dobbs & Burkert (2012)). Here, we find the average gas density to be $\sim 1 M_\odot \text{pc}^{-2}$. Beyond, the gas density decreases further. While it appears to reach a plateau of $2 \times 10^{-2} M_\odot$ around 12 kpc, we recall that we have not detected much significant emission beyond $r \approx 10$ kpc.

We have fitted Gaussian profiles $g_i(z) \propto \exp[-(z - z_{0,i})^2 / 2\sigma_i^2]$ with means $z_{0,i}$ and standard deviations σ_i to the gas density distribution in the same galacto-centric rings i as before by minimising the χ^2 over all rings,

$$\chi^2 \equiv \sum_i \sum_\gamma \frac{\langle n_{\text{H}_2, \alpha\beta\gamma} \rangle_{\alpha\beta, i} - g_i(z_\gamma)}{\bar{\sigma}_i^2}. \quad (19)$$

Here, $\langle \dots \rangle_{\alpha\beta, i}$ denotes the averaging over all grid points $\alpha\beta$ in the i -th ring. We have fixed the uncertainty $\bar{\sigma}_i$ to 0.15 of the maximum of $\langle n_{\text{H}_2, \alpha\beta\gamma} \rangle_{\alpha\beta, i}$ for that particular ring i . For most rings, the

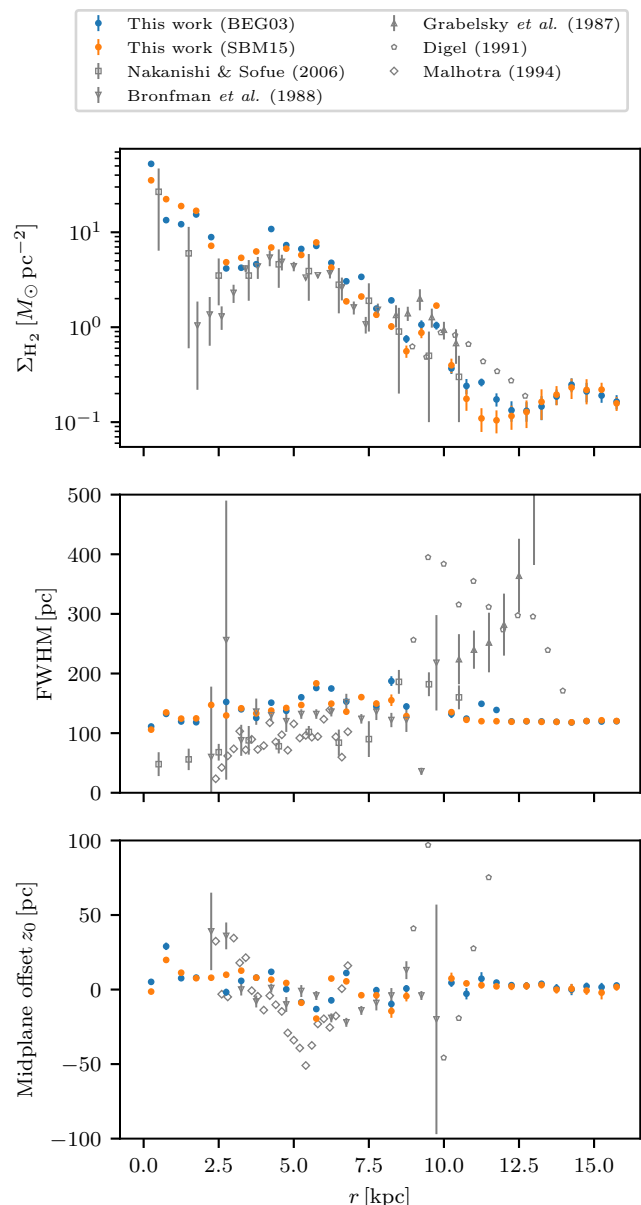


Fig. 8. Radial profiles of the surface mass density Σ_{H_2} (top panel), FWHM of the z -profile (middle panel) and midplane offset (bottom panel). We compare the results for both our gas flow models (BEG03 and SBM15) with the results of earlier studies: Grabelsky et al. (1987), Bronfman et al. (1988) and Nakanishi & Sofue (2006).

Gaussian profile is a fair approximation, $\chi^2 < 1$. (Of course, different z will be correlated, hence χ^2 is usually < 1 .) For other rings, however, the average profile in z is only poorly described by a single Gaussian (see also Dame & Thaddeus 1985). We have thus removed these bins. We stress that the ensemble of samples from the posterior consists of full 3D distributions. Also uncertainties and correlations contained, so allow for any statistical analysis beyond the axisymmetric quantities and simple error estimates.

We show the FWHM, that is $2\sqrt{2\log 2}\sigma$, a measure of the vertical extent of the gas distribution, as a function of galacto-centric radius in the middle panel of Fig. 8 and compare to a number of previous estimates. We note that our reconstructed gas densities seems to be more extended vertically, at least in

the inner few kiloparsecs. Note that Pohl et al. (2008) does not determine this parameter but instead uses it as an input for the analysis.

In the bottom panel of Fig. 8, we show the dependence of the midplane offset z_0 on the galacto-centric radius and again compare to a number of previous estimates. While the general trend with galacto-centric radius is the same as that seen in previous studies, our error bars are consistently smaller. We stress that the ensemble of samples from the posterior consists of full 3D distributions. Also uncertainties and correlations contained, thus allowing for any statistical analysis beyond the axisymmetric quantities and simple error estimates.

4. Summary

We have presented a new deprojection of the CO line survey of Dame et al. (2001) with unprecedented spatial resolution of 62.5 pc. This is based on a Gaussian variational Bayesian inference which allows exploring the posterior distribution of this high-dimensional inference problem. While we have assumed correlations in configuration space to exist, we have not assumed any particular power spectrum, but determined the power spectrum during the reconstruction. We have considered two gas flow models, that both take into account the presence of the Galactic bar, one based on a simulation of the gas flow in a predetermined potential (Bissantz et al. 2003)[BEG03], the other based on a model for gas carrying orbits in the bar potential (Sormani et al. 2015)[SBM15].

Our results are the three-dimensional distribution of molecular gas, assuming a fixed X_{CO} factor of $2 \times 10^{20} \text{ molecules cm}^{-2} (\text{K km s}^{-1})^{-1}$. We have made our mean gas maps and their uncertainty available to the community³. We have shown the mean and the standard deviation of the gas density projected onto the Galactic plane and compared with previous studies. Unlike those earlier studies, we have the capacity to distinguish between statistically significant structures and noise artefacts. We have found that some of the most prominent structures are influenced by the assumed spiral structure in the BEG03 gas flow model, but that significant coherent structures, some of which align with spiral arms (as for instance defined by parallax measurements of masers) are present in the SBM15 model as well. We have projected some radial profiles out of the 3D gas distribution and found the results of previous studies largely confirmed.

In the future, a couple of extensions of the current analysis are noteworthy. Having successfully applied our methodology to molecular line surveys to determine the H_2 density it would be interesting to apply it to surveys of atomic hydrogen, like the recently completed HI4PI survey (HI4PI Collaboration et al. 2016). While the HI distribution is known to show less clustering than molecular hydrogen, we are optimistic that the advantages of our approach carry over. In addition, a couple of shortcomings of the present study are due to our ignorance of the gas flow. If the velocity field could be determined at the same time as the gas density, such deficiencies could be remedied. We can envisage two ways to help regularise this underdetermined problem: Data from the above mentioned parallax measurements (Reid et al. 2019) could be included, thus providing at least a couple of loci to which the velocity field could be anchored. In addition, physical correlation between gas densities and flow velocities could link the reconstruction of both fields, of course, this would require additional model inputs.

References

- Ackermann, M., Ajello, M., Atwood, W. B., et al. 2012, *ApJ*, 750, 3
 Arras, P., Frank, P., Leike, R., Westermann, R., & Enßlin, T. A. 2019, *A&A*, 627, A134
 Athanassoula, E. 1992, *MNRAS*, 259, 345
 Baba, J., Saitoh, T. R., & Wada, K. 2010, *PASJ*, 62, 1413
 Bayes, M. & Price, M. 1763, *Philosophical Transactions of the Royal Society of London Series I*, 53, 370
 Binney, J., Gerhard, O. E., Stark, A. A., Bally, J., & Uchida, K. I. 1991, *MNRAS*, 252, 210
 Bissantz, N., Englmaier, P., & Gerhard, O. 2003, *MNRAS*, 340, 949
 Blei, D. M., Kucukelbir, A., & McAuliffe, J. D. 2016, *arXiv e-prints*, arXiv:1601.00670
 Blitz, L. & Spergel, D. N. 1991, *ApJ*, 379, 631
 Bolatto, A. D., Wolfire, M., & Leroy, A. K. 2013, *ARA&A*, 51, 207
 Bovy, J. 2015, *ApJS*, 216, 29
 Bronfman, L., Cohen, R. S., Alvarez, H., May, J., & Thaddeus, P. 1988, *ApJ*, 324, 248
 Clemens, D. P., Sanders, D. B., & Scoville, N. Z. 1988, *ApJ*, 327, 139
 Dame, T. M., Hartmann, D., & Thaddeus, P. 2001, *ApJ*, 547, 792
 Dame, T. M. & Thaddeus, P. 1985, *ApJ*, 297, 751
 Dobbs, C. L. & Burkert, A. 2012, *MNRAS*, 421, 2940
 Ferrière, K. M. 2001, *Reviews of Modern Physics*, 73, 1031
 Grabelsky, D. A., Cohen, R. S., Bronfman, L., Thaddeus, P., & May, J. 1987, *ApJ*, 315, 122
 Hastings, W. K. 1970, *Biometrika*, 57, 97
 Heyer, M. & Dame, T. M. 2015, *ARA&A*, 53, 583
 HI4PI Collaboration, Ben Bekhti, N., Flöer, L., et al. 2016, *A&A*, 594, A116
 Hou, L. G. & Han, J. L. 2014, *A&A*, 569, A125
 Jóhannesson, G., Porter, T. A., & Moskalenko, I. V. 2018, *ApJ*, 856, 45
 Kennicutt, R. C. & Evans, N. J. 2012, *ARA&A*, 50, 531
 Kewley, L. J., Nicholls, D. C., & Sutherland, R. S. 2019, *ARA&A*, 57, 511
 Knollmüller, J. & Enßlin, T. A. 2019, *arXiv e-prints*, arXiv:1901.11033
 Kolmogorov, A. 1941, *Akademiia Nauk SSSR Doklady*, 30, 301
 Kullback, S. 1968, *Information theory and statistics*
 Laplace, P. S. 1986, *Statist. Sci.*, 1, 364
 Leike, R. H. & Enßlin, T. A. 2019, *A&A*, 631, A32
 Miville-Deschênes, M.-A., Murray, N., & Lee, E. J. 2017, *ApJ*, 834, 57
 Nakanishi, H. & Sofue, Y. 2006, *PASJ*, 58, 847
 Nordlund, Å. K. & Padoan, P. 1999, in *Interstellar Turbulence*, ed. J. Franco & A. Carraminana, 218
 Ostriker, E. C., Stone, J. M., & Gammie, C. F. 2001, *ApJ*, 546, 980
 Persic, M., Salucci, P., & Stel, F. 1996, *MNRAS*, 281, 27
 Pettitt, A. R., Dobbs, C. L., Acreman, D. M., & Price, D. J. 2014, *MNRAS*, 444, 919
 Pohl, M., Englmaier, P., & Bissantz, N. 2008, *ApJ*, 677, 283
 Reid, M. J., Menten, K. M., Brunthaler, A., et al. 2019, *ApJ*, 885, 131
 Schuller, F., Urquhart, J. S., Csengeri, T., et al. 2021, *MNRAS*, 500, 3064
 Shu, F. H. 2016, *ARA&A*, 54, 667
 Sormani, M. C., Binney, J., & Magorrian, J. 2015, *MNRAS*, 449, 2421
 Sun, J., Leroy, A. K., Schrubba, A., et al. 2018, *ApJ*, 860, 172
 Szűcs, L., Glover, S. C. O., & Klessen, R. S. 2014, *MNRAS*, 445, 4055
 Wenger, T. V., Balsa, D. S., Anderson, L. D., & Bania, T. M. 2018, *ApJ*, 856, 52
 Wilson, R. W., Jefferts, K. B., & Penzias, A. A. 1970, *ApJ*, 161, L43

Appendix A: Semi-analytical gas flow model

Short of running our own hydrodynamical simulations of gas flow in a barred potential, we employ a semi-analytical approximation to the gas flow. It has been hypothesised by Binney et al. (1991) that gas in the potential of a rotating bar is drifting slowly towards the centre, moving on orbits from two classes of closed orbits, so-called x_1 and x_2 orbits. The transition from the outer x_1 orbits to the inner x_2 orbits is taking place via a shock structure that forms along a critical, cusped orbit. Beyond, the x_1 orbits are self-intersecting, but the gas is drifting on x_2 orbits instead. This picture was observed in early simulations (Athanasoula 1992), albeit with limited resolution and a somewhat different potential than assumed by Binney et al. (1991), and more recently confirmed for the same potential and with a high resolution simulation SBM15. Here, we adopt the potential of SBM15, but slightly adjust their parameters.

Specifically, we adopt a combination of a triaxial potential for the bar,

$$\rho(r') = \frac{\rho_0}{4\pi a^3} \frac{1}{(r'/a)^\alpha (1 + r'/a)^{\beta-\alpha}} \quad (\text{A.1})$$

with $r' = \sqrt{x^2 + (y/a)^2 + (z/a)^2}$ and a razor-thin disk potential generated by the surface mass density

$$\Sigma(R) = \Sigma_0 e^{-R/R_d}, \quad (\text{A.2})$$

R denoting the cylindrical galacto-centric radius. We adopt the following parameters: $\rho_0 = 0.69 M_\odot \text{pc}^{-3}$, $a = 1.8 \text{ kpc}$, $\alpha = 1.75$, $\beta = 3.5$, $\Sigma_0 = 1.3 \times 10^3 M_\odot \text{pc}^{-2}$ and $R = 4.5 \text{ kpc}$. We assume a pattern speed of $\Omega_p = 63 \text{ km s}^{-1} \text{ kpc}^{-1}$ for the rigidly rotating bar potential.

We solve the equations of motion for test particles in the combined potential using the `galpy` package⁴ (Bovy 2015). We find closed x_1 and x_2 orbits in the range of galacto-centric radius $\leq 4 \text{ kpc}$. Some examples are shown in Fig. A.1.

We have interpolated the velocity field between the points on the x_1 and x_2 orbits for galacto-centric radii $R \leq 4 \text{ kpc}$. While this works well for the regions inside the largest populated x_2 orbit and outside the smallest populated x_1 orbit, in between those orbits, the gas velocities are somewhat overestimated, see Fig. 5 of SBM15. We have therefore added a couple of nodes in the interpolation of the radial gas velocities to reach better agreement with Fig. 5 of SBM15.

Beyond 4 kpc, we have assumed gas to move on circular orbits and for the velocity to follow the ‘‘universal rotation curve’’ of Persic et al. (1996) with the updated parameters of Reid et al. (2019). A small suppression of 5% was necessary to make the rotation curve connect smoothly with the interpolation at $R = 4 \text{ kpc}$.

In the middle panel of Fig. 3, we have shown the radial velocity resulting from this semi-analytical gas flow model. Even though we have adopted slightly different parameters than SBM15, we refer to this model as the SBM15 model in the main text.

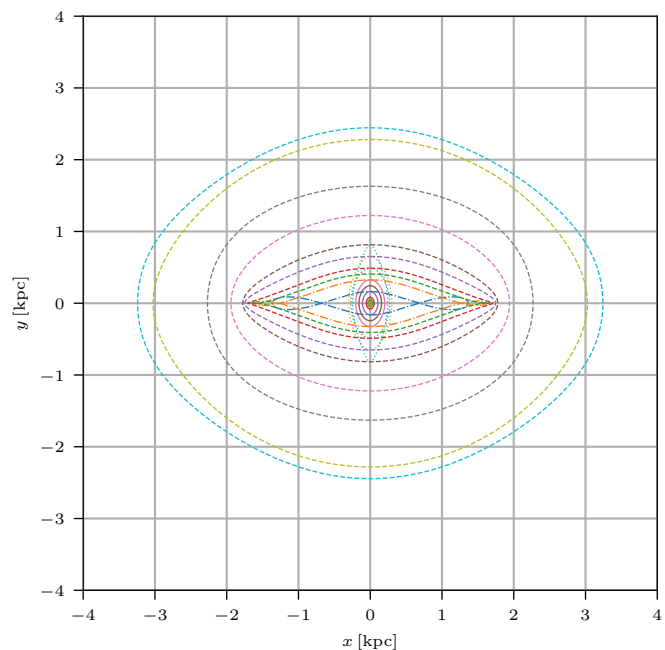


Fig. A.1. Some examples for x_1 and x_2 orbits found by solving for closed orbits in the rotating bar potential. The x_1 orbits are marked by dashed and dot-dashed lines and the x_2 orbits are marked by solid and dotted lines. Gas is assumed to be moving on only a subset of those, that is on the orbits marked by a solid or dashed line. Orbits beyond the largest shown orbit are assumed to be circular.

⁴ <http://github.com/jobovy/galpy>